Ion Pairing and Dielectric Decrement in Glycosaminoglycan Brushes

James D. Sterling[†*] Wenjuan Jiang[‡], Wesley M. Botello-Smith[‡], Yun L. Luo[‡*].

[†] *Henry E. Riggs School of Applied Life Sciences, Keck Graduate Institute, 535 Watson Dr., Claremont, California, 91711, United States*

[‡] *College of Pharmacy, Western University of Health Sciences, 309 E. Second St., Pomona, California, 91766, United States*

Correspondence: jim_sterling@kgi.edu or luoy@westernu.edu

ABSTRACT

Cell-surface polysaccharides are essential to many aspects of physiology, serving as a highly-conserved evolutionary feature of life and as an important part of the innate immune system in mammals. Here, as simplified biophysical models of these sugar-coatings, we present results of molecular dynamics simulations of hyaluronic acid and heparin brushes that show important effects of ion-pairing, water dielectric decrease, and co-ion exclusion. As in prior studies of macromolecular crowding under physiologically-relevant salt concentrations, our results show equilibria with electroneutrality attained through screening and pairing of brush anionic charges by monovalent cations at atomistic detail. Most surprising is the reversal of the Donnan potential obtained from both nonpolarizable and Drude polarizable force fields, in contrast to what would be expected based on electrostatic Boltzmann partitioning alone. Water dielectric decrement within the brush domain is also associated with Born hydration-driven cation exclusion from the brush. We observe that the primary partition energy attracting cations to attain brush electroneutrality is the ion-pairing or salt-bridge energy. Potassium and sodium pairing to glycosaminoglycan carboxylates and sulfates show similar abundance of contact-pairing and solvent-separated pairing. We conclude that in these crowded macromolecular brushes, ion-pairing, Born-hydration, and electrostatic potential energies all contribute to attain electroneutrality and should therefore contribute in mean-field models to accurately represent brush electrostatics.

INTRODUCTION

Glycosaminoglycans (GAGs) are macromolecular linear polysaccharides whose interactions are governed largely by electrostatic salt-bridges between their anionic charges and cations and/or cationic residues of proteins[1–3]. As cell-surface and extracellular macromolecules, GAGs play important roles in angiogenesis, inflammation, immunity, and cell penetration processes.[4–8] As

multivalent macromolecules, heparan sulfate proteoglycans (HSPGs) promiscuously bind to many proteins, a long list of at least 300 growth factors, chemokines and cytokines known as the interactome. The binding depends on ion pairing between the anionic heparan sulfates (HS) and the basic domain sequences of the proteins; interactions which can be considered targets for therapeutic intervention.[9–11] Based on these electrostatic interactions, heparin has a long history of application in affinity chromatography.[12,13] Recently, HSPG-binding has been shown to mediate cell uptake of tau protein, α-synuclein, and β-amyloid aggregates elucidating a role of GAGs in neurodegenerative disease as well as in viral infectious disease including the SARS-CoV-2 virus.[14–17] As intrinsically-disordered macromolecules, GAGs can also partition ions and cationic macromolecules to form liquid-liquid phase separations and coacervates.[18] In addition to heparin and HS, other GAGs include keratan/chondroitin sulfate which uniquely include N-acetylgalactosamine in each disaccharide, and hyaluronic acid which is uniquely non-sulfated among the GAGs.

Glycosaminoglycans, other proteoglycans, and mucins are typically 100s of kilodaltons to over 10 megadalton macromolecules that form a glycan-rich region outside the membrane of cells called the glycocalyx. The glycocalyx at mucosal surfaces, endothelial surfaces, tissue interfaces, as well as tumor cell surfaces act as a set of tethered macromolecular polyelectrolytes, forming microscale anionic domains that partition ions to attain electroneutrality. Several studies have shown that the net/integral anionic charge density often plays a more important role in binding activity than specific sulfation patterns.[1,2,15,19] A number of important biophysical effects have been studied in efforts to elucidate quasi-equilibrium geometry, composition and electrostatic state of the glycocalyx. Biophysical models of the glycocalyx as polysaccharide hydrogels, soft diffuse interfaces, or polyelectrolyte brushes have been developed and several research groups have recently applied electrokinetic methods to measure ionic conductivity within the polymer region[19–24]. These measurements often utilize fitting with mathematical mean-field models to determine polymer density, electrostatic/Donnan potential and, if charge densities are not dilute, ion-pair binding constants to match measured surface conductivity[25–27].

Here, we use all-atom molecular dynamics (MD) simulations at the nanoscale to identify emergent properties that can be used in mean-field microscale models to improve our understanding of the glycocalyx. We model the glycocalyx as a brush which is defined as a surface coating of tethered polymers. Here, the GAG polymers are charged and linear resulting in a solvated polyelectrolyte brush with only NaCl or KCl. This approach presents a model that can be rigorously studied to characterize glycocalyx biophysics in the absence of the complicating reservoir of additional biomolecules that are found in the glycocalyx around living cells.

The first section below presents the computational methods and setup for the simulation of hyaluronic acid and heparin brushes bounded by NaCl or KCl solutions. The results and discussion section follows with a report on the collapse of the brush from a fully-extended state and the resulting charge densities in the brush and bulk regions. We then evaluate the electrostatic potential

in the brush relative to the bulk salt, also called the Donnan potential, using the Particle Mesh Ewald (PME) method and we compute the dielectric decrement of the water in the two regions and estimate the Born hydration energies for the cations in those regions. The role of ion-pairing of the cations to specific oxygen atoms of the anionic carboxylates and sulfates in the GAGs is then presented. We show that all-atom MD simulations of hyaluronic acid brushes can produce consistent brush electroneutrality with anion exclusion using both CHARMM36 additive all-atom carbohydrate force fields and CHARMM-Drude polarizable force fields for carbohydrates.[28–32] The effect of pair-specific Lennard-Jones parameters on the Donnan potential, ion pairing, dielectric constant, and GAG brush topology were evaluated for Na^+ and K^+ interactions with carboxylate and sulfate anions. We conclude by postulating a cation-centric mean-field model for the GAG brushes that includes electrostatic, Born-hydration, and ion-pairing energies that govern quasi-static electroneutrality.

COMPUTATIONAL METHODS

Simulated Systems: MD simulations to assess the variability of brush integral charge density were performed by using uniform-disaccharide models of the least-charged (-1e per disaccharide) and most highly-charged (-5e per disaccharide) GAGs; hyaluronic acid and oversulfated heparin as used by Stopschinski *et.al*. in their study of sulfation associated with Tau internalization.[15] Under physiological pH, the oversulfated heparin disaccharide, GlcA2Sα4GlcNS3S6Sα4, has five negative charges and the hyaluronan disaccharide, GlcAβ3GlcNAcβ4 has one negatively-charged carboxylate. Simulations were initially conducted for different length GAG brushes in 200mM NaCl solutions. (**Figure S1**). The final brush model we considered was a grid of GAG molecules of 16-disaccharide units tethered by a fixed oxygen atom of the (1→4) glycosidic bond in the middle of the molecules that are placed in the middle (defined as horizontal axis z = 0) of the orthorhombic periodic box of 480Å in length. **Figure 1** shows the molecular structure of the oversulfated heparin. A total of eight 16-disaccharide length brush systems with different salt or salt concentrations were simulated. Detailed information about each system is shown in **Table S1a**.

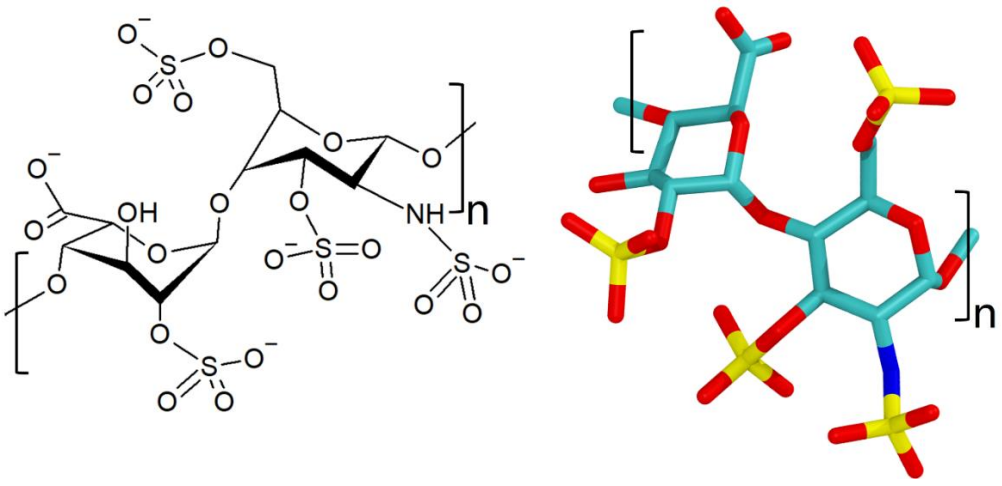

Figure 1: Molecular structure of oversulfated heparin glycosaminoglycan with repeating disaccharide GlcA2Sα4GlcNS3S6Sα4. The left image shows the 2D chemical structure and the right image shows the 3D structure using the color scheme: oxygen in red, nitrogen in blue, sulfur in yellow, carbon in cyan, hydrogen not shown for clarity.

We emphasize that there is no solid surface or substrate to which the molecules are tethered. The brush is formed by a 20Å × 20Å array of four of these GAG molecules (**Figure 2**) in the fully extended initial state (t=0, ~160Å length since each disaccharide is ~10Å long), and in the collapsed quasi-steady state (t=100ns). The periodic boundary conditions (PBC) are applied which create an infinite lattice of the brush in the x-y plane that is surrounded by saline solution of near 250 mM (Debye length near 6Å). Ion-specific behavior is assessed by simulating NaCl and KCl solutions in both the hyaluronan and heparin GAGs to give four salt-GAG combinations. Our simulations represent tethered strong polyelectrolytes in the extended ionizable osmotic-brush regime.[27,33,34] GAGs are moderately strong acids. The pKa values of the solvated sulfates and carboxylates are expected to remain in the range of 0.5-1.5 and 2-3.5 respectively.[35] Our largest brush model contains 64 carboxylates and 256 sulfates so at a pH of 7 it would require at least 10 times our system size before one carboxylate would likely be protonated. Electroneutrality is therefore attained solely through inclusion of exactly the same number salt cations as GAG acidic groups plus salt anions.

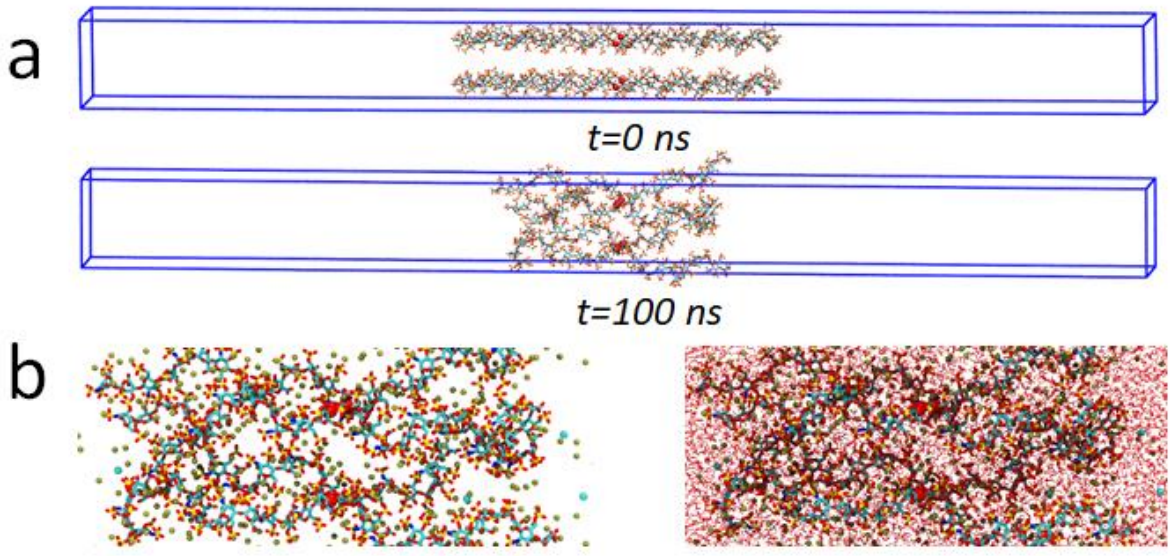

Figure 2. Representative simulation system (a) System with initial fully-extended four 16-disaccharide GAG molecules tethered at center (z=0) in unit cell forming a 40Å × 40Å × 480Å x-y-z (depth-height-width) simulation box. The initial heparin extent is approximately z = -65Å to +65 Å with saline solution occupying region from z = -240 Å to +240Å. Upon attaining quasi-steady state, the brush collapses to span approximately z = -50Å to +50Å. (b) System shows ions (Cl- is Cyan and K^+ is Brown) on the left and water molecules on the right. The four large red spheres in VDW mode represent the oxygen at the glycosidic bonds at the center of the heparin that are tethered.

Force Field and Molecular Dynamics Simulation Setup: The heparin and hyaluronic acid glycan models were prepared from CHARMM-GUI module "Glycan Reader & Modeler" respectively.[41–44] Simulations with nonpolarizable force fields were executed in GROMACS (version 2016.4)[45] with the CHARMM36 additive force field and CHARMM TIP3P water[46]. Each system was solvated with total salt of 200mM of KCl or NaCl in the simulation box. Simulations were performed both with and without Nonbonded FIX (NBFIX) corrections for the K^+/COO^- and K^+/OSO_3^- ion pairs. These modified Lennard-Jones parameters were previously optimized by Yoo and Aksimentiev[40] using osmotic pressure simulations developed by Luo and Roux[38] for cation-acetate and cation-phosphate in crowded aqueous salt solutions. Note the phosphate terminal oxygen has the same nonbonded parameters as sulfate terminal oxygen in CHARMM36 force field. Simulation of Na^+/COO- and Na^+/OSO_3^- ion pairs utilized the CHARMM36 force field default parameters that included the NBFIX corrections we previously obtained from osmotic pressure data on sodium acetate and electrophoresis data on lipid vesicles.[47] As an initial assessment of the role of polarization, the hyaluronic acid system was also simulated using the polarizable Drude force field for carbohydrates and ion (version 2019) with SWM4-NDP water model.[48] The system was prepared using CHARMM program version 44b2 and simulated using NAMD2.13. The default NBFIX corrections for Drude Na^+/COO^- and K^+/COO^- ion pairs have also been optimized using osmotic pressure calculations (Lemkul and Noskov, unpublished) and hence included in current simulations. Those ionic pair force field parameters used in this study are summarized in **Table S1b**. The force field parameters can be downloaded from http://mackerell.umaryland.edu/charmm_drude_ff.shtml. The Drude version used in this study is also provided as **Supporting Materials**. Standard MD simulation protocols are presented in **Supporting Information**. Coulomb interactions were calculated using the particle-mesh Ewald (PME) algorithm.[49] Electrostatic potentials were obtained using the VMD PMEPot plugin[50] to compute a 3D electrostatic potential map $\phi(r)$ based on the selected charged atoms in the simulated system $\rho_i(r)$ by solving $\nabla^2\varphi(r) = -4\pi\sum_i \rho_i(r)$ on a 1Å resolution grid.

RESULTS AND DISCUSSION

Charge density and length of brushes. Heparin lengths of 6, 8, 10, 12, 14 and 16 disaccharide units were simulated with NaCl for 100ns in NVT ensemble with constant volume for the simulation box (**Table S1a,** System II), and the charge density profile of the GAGs was observed to be quite non-uniform for the shorter lengths while the longer 12 and 16 disaccharide brushes approached nearly a uniform charge density of about 3M with superimposed oscillations associated with the disaccharide units (**Figure S1**). For each of the brush lengths, the number of chloride ions is fixed at 93 over the entire volume to provide 0.20M. However, since these co-ions are excluded from the brush the actual concentration outside the brush increases with brush length reaching 0.26-0.28 M for the 16 disaccharide unit brushes presented here.

The brushes were observed to collapse to a statistically-invariant thickness within 50ns, hence we chose 100ns and 16 disaccharides as sufficient in temporal and spatial extent that the internal brush structure could be characterized as quasi-steady and near-uniform. An example of a charge density profile along the z-axis (x-y averaged) for 16-disaccharide heparin in 0.26M KCl (**Table S1a**, System I) is shown in **Figure 3**. Although the simulated system is maintained as electroneutral and ~3M potassium nearly cancels the negative GAG charge in the brush, there are small variations of net charge density in the brush that are less than 10% of the anionic brush charge density as seen by the brown curve. The bumps at the brush edges in the brown curve show a double-double layer of positive charge just outside of the brush and negative charge just inside the brush that is expected under diffuse-layer Boltzmann partitioning.

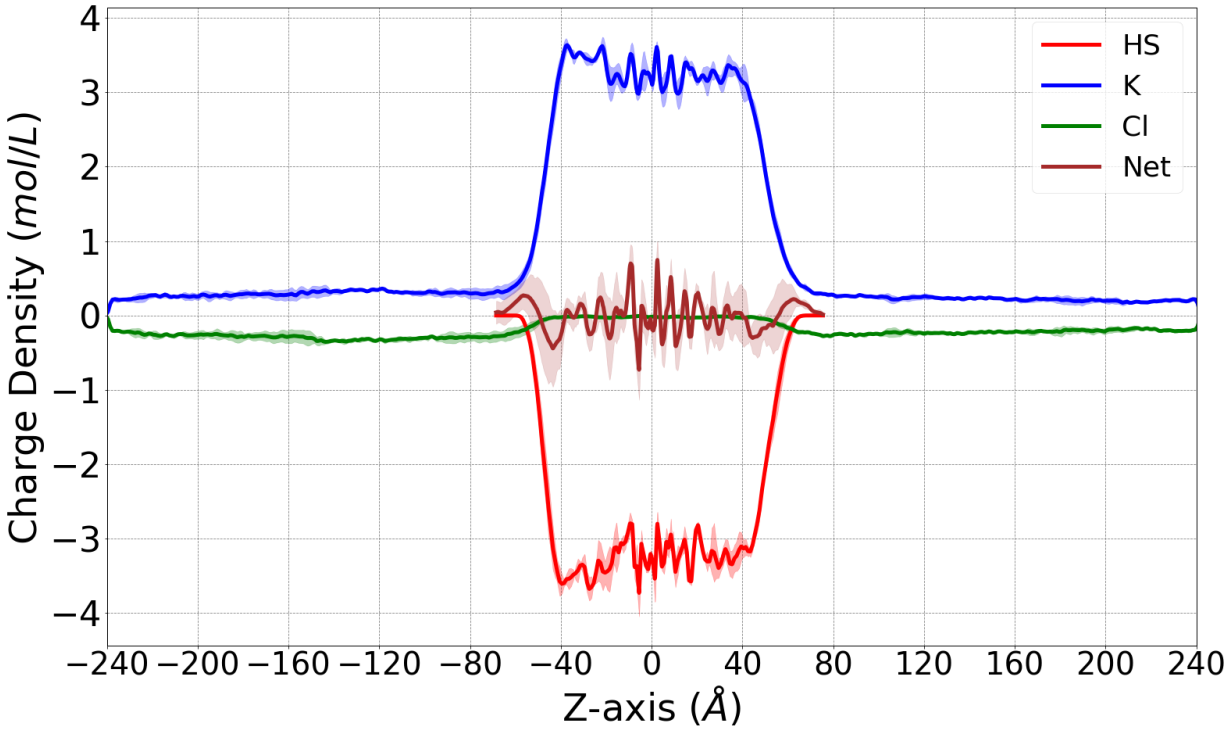

Figure 3. The quasi-steady charge density profile of heparin in 0.26M KCl, calculated using VMD VolMap function averaged over 100ns simulation. The charge density in moles/liter is plotted as a function of distance from the center of the brush for the oversulfated heparin in the red curve (HS), the potassium in blue (K), chloride in green (Cl) and the net charge density is shown by the brown curve (Net). The standard deviation for each density curves are shown in shaded regions calculated from 70-80ns, 80-90ns and 90-100ns trajectories.

A summary of the GAG Brush simulation results is presented in **Table 1**, which documents the brush-collapse by thickness and density as well as the bulk salt concentration that results upon co-ion exclusion. The polymer length is defined as the distance between the brush-edges averaged over the final 30ns of simulation and brush-edges are defined as the locations where the negative GAG charge-density value is equal to the average of the maximum and minimum values across the entire domain.

Table 1. Results of GAG Brush Simulations after 100ns AA simulations.

GAG	Salt	Bulk Salt Conc. (M)	GAG charge (M)	GAG Mass (Dalton)	Polymer Length (Å)	Initial Polymer Length (Å)	Polymer Length Fraction	Brush Density (g/L)
Hyaluronan	NaCl	0.28	0.51	6071.05	129.7	157.8	0.82	194.32
	KCl	0.28	0.49	6071.05	135.8	160.3	0.85	185.59
Heparin	NaCl	0.27	2.78	10457.66	119.3	145.1	0.82	363.90
	KCl	0.26	2.93	10457.66	113.2	146.0	0.78	383.51

*polymer lengths were averaged over last 30ns in each system.

Donnan potential. We then calculated electrostatic potential for the various combinations of salt with 16-disaccharide GAGs using CHARMM36 and Drude force fields (**Table S1b**). The convergence of electrostatic potentials was monitored over time (**Figure S4**). Averaged and standard deviation of potential profiles are presented in **Figure 4** for the hyaluronan system. In contrast to the near-uniform brush charge of Figure 3, this electrostatic distribution is not as smooth and is a result of the composite summing of electric potential contributions from all ion charges and all partial-charges associated with GAG atoms and water partial charges. Nonetheless, a consistent result is that the brush region holds a positive potential relative to the bulk salt solution.

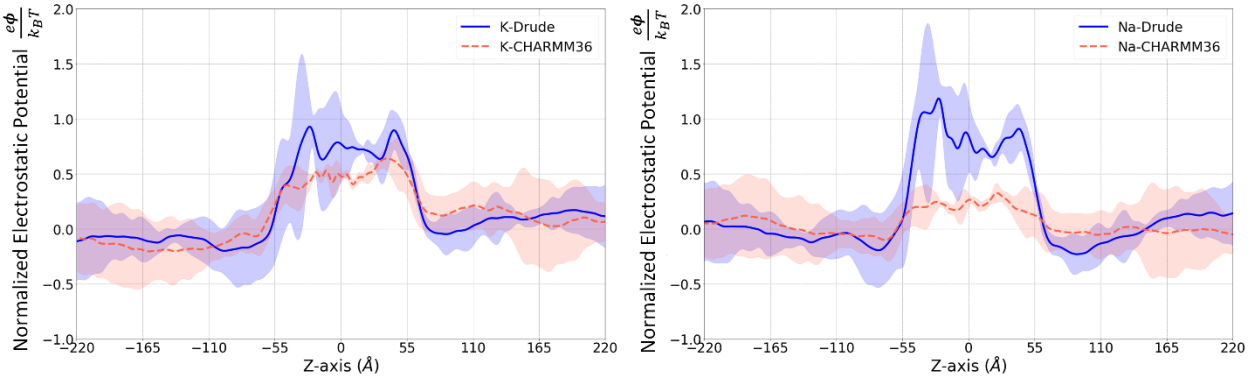

Figure 4: Hyaluronan-Cation Particle Mesh Ewald (PME) electrostatic potential for nonpolarizable CHARMM (new NBFIX for K^+/COO^- see **Table S1b**) and polarizable Drude-model simulations. Curves are shifted to provide average of zero/ground baseline outside of the brush. (i.e. defined as the region where the net potential is less than the half-maximum difference between the net potential peak and its minimum). The solid blue curves show Drude force field results and the dashed pink curves show CHARMM36 additive force field results with the blue and pink shaded region for the standard deviation calculated based on 70-80ns, 80-90ns and 90-100ns trajectories for each system.

Surprisingly, the Donnan rule does not apply; even though the brush excludes all anions and the net brush charge is neutralized by cations, the net electrostatic potential is positive relative to the surrounding saline solution. We quantify the effective brush potential for all conditions and the results are reported in column 4 of **Table 2**. In the case of the dashed blue curve of Figure 4 for HA-K^+ using the CHARMM36 force field, the average potential is 0.44±0.03 where the standard deviation is the temporal variation of the spatial average for three time points 40, 80, and 100ns. Therefore, the net relative brush potential corresponds to positive 11.7 ± 0.8 mV for the thermal voltage of 26.7 mV (at temperature of 310.15K).

Is the inverted electrostatic potential an artifact of the all-atom partial charge model in CHARMM? We explored this question by using both non-polarizable and polarizable force field models in our simulations. Optimization of nonpolarizable force fields in MD is a topic of considerable active research where various ionic charge scaling electronic continuum correction (ECC) models as well as adjustments of LJ parameters between specific ion-pairs using nonbonded fix (NBFIX) models have been developed, in part to address excessive ion-pairing that has been observed in some MD simulations.[64–66] Donnan potential is largely dictated by ion pairing potential. We found that applying the new NBFIX correction for K^+/COO^- and K^+/OSO_3^- ion pairs (**Table S1b**) reduced the number of contact ion pairs, hence resulted a ~3-fold decrease in positive Donnan potential of heparin-KCl system (**Figure S5**). This new Donnan potential is more consistent with the potential obtained from heparin-NaCl system using default CHARMM36 NBFIX for Na^+/COO^- and Na^+/OSO_3^- ion pairs.

To assess the influence of polarizability on Donnan potential, we simulated the hyaluronan-potassium system using a recently-developed CHARMM Drude polarizable model for carbohydrates. Interestingly, including polarizability produced similar inverted Donnan potentials with even larger magnitudes as shown in **Figure 4** and we see that the polarization effect is more pronounced for sodium than potassium. Therefore, our quantitative results are indeed dependent on the model but the inversion of the electrostatic potential of the brush did not change. We note that the contrast between sodium and potassium Donnan results are most pronounced in heparin where we see the largest positive Donnan value for the System I potassium-heparin brush and that the only negative Donnan potential is observed for our System II sodium-heparin brush (**Table 2** column 4).

Dielectric Decrement. Perhaps these inverted Donnan potentials in GAG brushes should not be surprising. Similar effects are observed in colloidal systems and nanoscale solid-liquid interfaces where water confinement and dispersion forces become important.[51–55] The behavior of water in crowded environments is indeed quite different than bulk water. Fundamental spectroscopic studies combined with MD simulations have recently elucidated the nature of water's dipole reorientation time in crowded environments and the corresponding decrement in the dielectric constant.[56–61] Not only do water dielectric decrements appear around charged groups and ions, but ion hydration effects also control ion-pairing that also affects the electrostatics.[62,63]

We computed the dielectric constant of the water for each brush simulation using the following equation for the relative permittivity ε given the permittivity of vacuum ε_o, Boltzmann constant k_B, temperature T, and dipole moment M of the water molecules within the available volume V.

$$\varepsilon = 1 + \frac{\langle M^2 \rangle - \langle M \rangle^2}{3\varepsilon_o V k_B T} \qquad \text{Eq. (1)}$$

The dielectric constant for the four GAG simulations are shown as a function of the distance from the center of the brush in **Figure 5**. The dielectric constant for the hyaluronan cases is observed to fall from around 62 outside the brush to around 50 within the brush. Similarly, for heparin, the constant falls from around 60 to a minimum around 35 within the brush. The fact that our solution phase exhibits a lower dielectric constant than bulk water is expected due to the high salt content as well as the temperature of 310.15K.

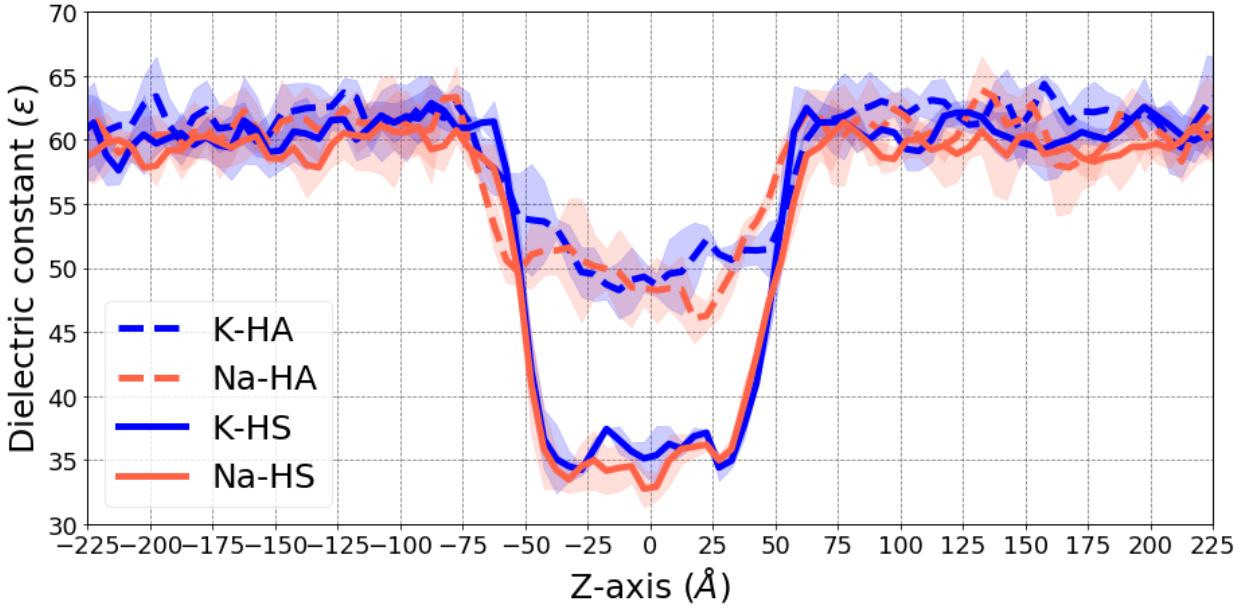

Figure 5. Dielectric constant within 5Å length slabs in the z-direction averaged over the 40Å x 40Å x-y domain; smoothed over ~1 disaccharide using a 10Å uniform window. The standard deviation for each system is shown in the shaded region calculated from 70-80ns, 80-90ns and 90-100ns trajectories.

Ion pairing in the brushes. The high charge densities in the brushes result in substantial ion pairing in the form of contact ion pairs (CIP) and solvent separated ion pairs (SIP).[67,68] As a first approximation, one might consider ion-pairing to fixed charged GAGs to provide a neutral pair such that the brush Donnan potential would be determined by the free ions in the brush that would be Boltzmann-partitioned from the bulk solution. This type of Donnan rule has long been applied in brush models with ionizable charged groups to consider pH effects under the assumption that

free hydronium is Boltzmann-partitioned.[20–22,26,69] In our simulations, the use of physiological pH and salt concentration values imply million-fold fewer hydronium than salt ions; so hydronium is not present in our MD simulations.

Radial distribution functions (RDF) of the cation-anion interactions typically display two peaks corresponding to the large CIP and SIP ion pair populations and the well corresponding to an energy barrier between them. **Figure 6** presents the RDF plots for the cations as they pair with the oxygen atoms associated with sulfates and carboxylates using the CHARMM36 with NBFIX. For K^+ pairing, CIP occurs for separation between the oxygens of less than about 3.4Å while SIP occurs for separation between 3.4Å and 5.9Å. Similarly, for Na+ pairing with these oxygen atoms, CIP occurs for separation between the oxygens of less than about 3.1Å while SIP occurs for separation between 3.1Å and 5.5Å. These results are consistent with the models of ion-pairing described by Marcus and Collins that are associated with negative free energy of binding driven by entropic gain of released water when similarly-hydrated ions pair.[67,70,71]

Another important feature seen in **Figure 6** is that cation-pairing to both GAG carboxylate oxygens and sulfate oxygens of heparin are present in CIP and SIP forms in similar quantity. In other words, the area under the curves for CIP and SIP forms are quite similar for all pairings. Finally, we note that the 3-O-sulfates and 6-O-sulfates show more CIP pairing than the 2-O-sulfates for both potassium and sodium; which could play a role in the distinct regulatory roles that heparin and sulfotransferases play in biology.[72,73] A more customary treatment of RDFs based on the central carbon atom of the carboxylate or sulfate is shown in **Figure S2** where the ion-specific behavior is quite clear. In **Figure S3**, a direct comparison of the RDFs of hyaluronan carboxylate-cation pairing to the central carbon and the oxygen atoms are shown and sodium is observed to have a higher SIP/CIP ratio than potassium.

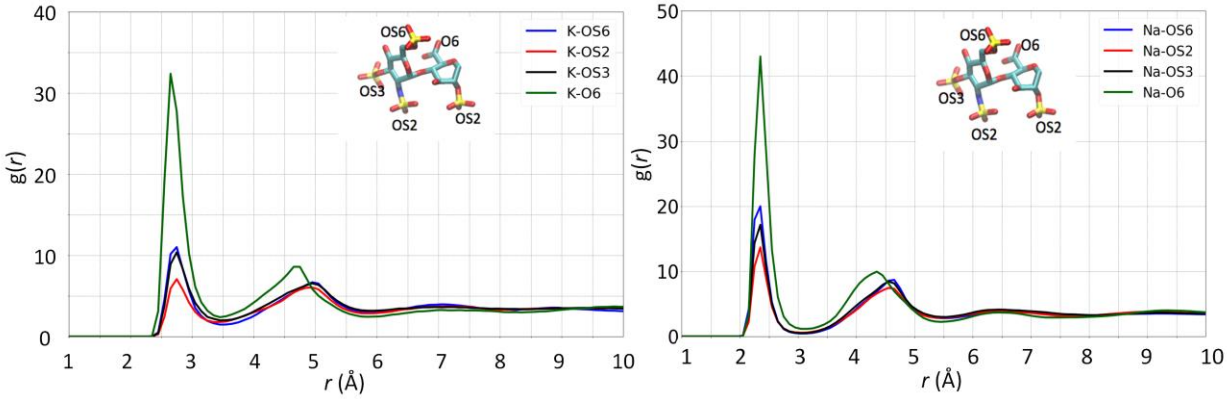

Figure 6. Radial distribution functions (RDF) of cations K^+ and Na^+ with sulfate oxygen and carboxyl oxygens in heparin systems. RDF curves were calculated from System I and II (CHARMM36 force field) for ion pairs of K^+/COO^- (new NBFIX), K^+/OSO_3^- (new NBFIX), Na^+/COO^-(CHARMM36 NBFIX), and Na^+/OSO_3^-(CHARMM36 NBFIX). See NBFIX values in Table S2. The curves represent the cation interactions with oxygens on: the 6-carbon carboxyl of

the GlcA saccharide (blue), the 2 carbon sulfate of either the GlcA or GlcN saccharide (red), the 3 carbon sulfate on the GlcN saccharide (black), and the 6-carbon sulfate of the GlcN (green).

These ion pairing results might suggest that modelling of CIP and SIP populations could directly apply the Eigen-Tamm law of mass action kinetics.[74] However, this approach is complicated by the fact that many ions are shared by multiple counterions, making the definition of concentrations ambiguous. This effect is clearly seen in **Figure 7** where snapshots of two potassium ions near the heparin brush are shown. The inter-molecularly shared potassium ion shown on the left figure is seen to be within CIP distance of three sulfate oxygens (2.79, 2.89 and 2.66 Å) and within SIP distance of another sulfate oxygen. Similarly, the intra-molecularly shared potassium shown on the right figure is seen to be within CIP distance of one carboxylate oxygen (2.63 Å) and one sulfate oxygen (2.71 Å).

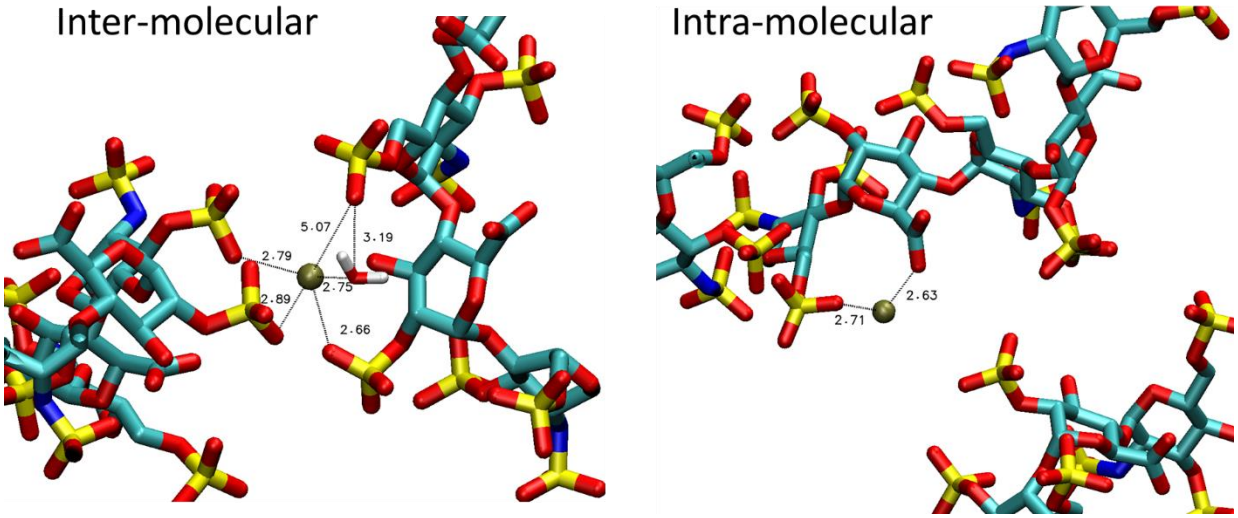

Figure 7: Ion-pairing in crowded GAG brush. Snapshot images of potassium ion-pairing to heparin (CHARMM force field for K^+/COO^- (new NBFIX) and K^+/OSO_3^- (new NBFIX)). Simultaneous contact- and solvent-separated ion pairing to sulfate oxygens (left) and simultaneous pairing to carboxylate oxygen and sulfate oxygen (right).

Relation with mean-field theory. A principal aim of this study is to characterize emergent behavior of GAG brushes to support microscale mean-field modeling through understanding of the equilibrium biophysics of the brushes. We observe both ion-pairing and dielectric decrement such that the equilibrium attained across the brush-solution interface can be represented by generalized Boltzmann partitioning that includes ion Born-solvation energy associated with the dielectric decrement, as well as the ion-pairing energies of cations with anionic brush charges. Minimization of free energy, or equivalently, integration of a steady-state Born-modified Poisson-Nernst-Planck (PNP) model with ion-pair binding yield such a generalized Boltzmann distribution as shown in equation (2).[54,75,76]

$$c_{i,b} = c_{i,o} \exp\left\{-\frac{W_i}{k_B T}\right\} = c_{i,o} \exp\left\{-\frac{q_i \varphi_b}{k_B T} - \frac{-\Delta G_i^s}{k_B T} \frac{\epsilon_w}{\epsilon_w - 1}\left[\frac{1}{\epsilon_b} - \frac{1}{\epsilon_o}\right] - \frac{\Delta \mu_i}{k_B T}\right\} \qquad \text{Eq. (2)}$$

The three terms represent the contributions of work done in partitioning of ion *i* from the solution phase represented by the *o* subscript, to the brush represented by the *b* subscript, due to electric potential, Born hydration, and ion-pairing, respectively. The electrostatic partitioning represents the ion charge q_i in brush potential φ_b relative to the solution phase using the simulation results for PME potential. In the absence of any dielectric decrement or ion-pairing, the brush potential could be considered to be the Donnan potential. The Born hydration term is based on the dilute experimental hydration energy of the ion ΔG_i^s where the dielectric constant of water is ε and the subscript *w* indicates the dilute value and the low value in the brush causes the ion to prefer to partition out of the brush into the higher dielectric water. The final term is the excess chemical potential difference $\Delta\mu_i$ across the interface that represents the ion-pair binding free energy and any ion-GAG interactions not associated with ion pairing. Ion-pair RDFs have been generated using MD and the relationship to Eigen-Tamm binding constants is described by Fennel *et al.* [77] for ion pairs and by Chen and Pappu[78] for clusters of up to 6 ions.

In **Table 2**, we report average values of these three energy terms from our GAG brush simulations. Column 3 contains values of the total partitioning energy that is required to attain electroneutrality in the brush and is equivalent to the naïve dimensionless Donnan potential that would be the electrostatic potential in the brush if the partitioning was entirely due to the balance of electrophoresis and diffusion. The fourth and fifth columns show the non-negative electrostatic potential energy and the positive Born hydration energy difference between the solution and the brush. The Born hydration energy is computed using the experimental hydration free energies ΔG_{Na}^s = -424 kJ/mol and ΔG_K^s = -352 kJ/mol. The cation binding free energy is computed as the residual required to satisfy the energy balance of the equation above and is shown in the final column. We see that both electrostatic and hydration effects tend to repel cations and that the excess energy required to overcome these effects and attain electroneutrality is the substantial negative binding energies of ion-pairing. We observe that in contrast to our initial expectations, the electrostatic potential contributes the least energy to the cation partition energy.

Table 2. Energy contributions to cation partitioning after 100ns AA simulations.

GAG	Salt	Total Partitioning Energy of Cation $\frac{W_i}{k_B T}$	PME Brush Potential Energy $\frac{q_t \varphi_b}{k_B T}$	Cation Born Hydration Energy Difference $\frac{-\Delta G_i^S}{k_B T}\frac{\epsilon_w}{\epsilon_w - 1}\left[\frac{1}{\epsilon_b} - \frac{1}{\epsilon_o}\right]$	Brush H_2O Dielectric Constant ϵ_b	Solution H2O Dielectric Constant ϵ_o	Cation Binding Energy $\frac{\Delta \mu_i}{k_B T}$
Hyaluronan	NaCl	-0.62	0.17±0.06	0.53±0.2	50.7±2.1	60.4±2.5	-1.32±0.2
	KCl	-0.56	0.44±0.03	0.46±0.2	51.2±2.9	61.8±1.9	-1.46±0.2
Heparin	NaCl	-2.34	-0.62±0.27	1.62±0.6	37.5±4.7	59.1±2.6	-3.35±0.6
	KCl	-2.41	0.96±0.14	1.36±0.5	37.9±4.2	60.5±2.1	-4.73±0.5

*The standard deviations for PME Brush Potential energy were calculated over three blocks from 0 to 40ns, 80ns, and 100ns for each system. The standard deviations for brush H_2O and solution H_2O dielectric constants were computed over the corresponding z-axis region, respectively. The cation binding energy and total partition standard deviation followed the rule of propagation of uncertainty.

Consider the magnitude of the cation binding energies reported in the final column of **Table 2**. Note that the magnitude of the binding energy appears to correlate with the number of anionic charges per disaccharide unit. If the binding is dominated by ion-pairing, the hyaluronan cation binding energy can be identified as the net cation-carboxylate binding energy that yields dimensional values of $\Delta\mu_{Na\text{-}COO}$ = -3.40kJ/mol and $\Delta\mu_{K\text{-}COO}$ = -3.76kJ/mol. Since heparin has the same carboxylate content as hyaluronan, in the absence of cooperativity of binding, the cation-heparin binding energy can be estimated as comprising 1/5 carboxylate binding energy and 4/5 sulfate binding energy. Here, the assumption is also made that the cation-sulfate binding energy is the same regardless of the sulfate glycan site, O-sulfation, or N-sulfation. Using this approach to solve for the average cation-sulfate binding energy, the ion-pair binding energies are presented in **Table 3**. Further evidence that ion-pairing dominates the binding is provided by simulations of hyaluronan with neutralized GAG anions as shown in **Table S1a** systems V and VI. The result is that chloride anions are no longer excluded from the brush and the PME potential is negligible.

Table 3. Approximate ion pair binding energy.

$\Delta\mu$ (kJ/mol)	COO^-	SO_4^-
Na^+	-3.40±0.3	-1.31±1.0
K^+	-3.76±0.3	-2.11±0.8

These results are consistent with the trends observed in the RDFs showing that carboxylates bind the cations more strongly than the sulfates. Attempts to develop more quantitative stoichiometric binding models using effective dissociation constants in an Eigen-Tamm kinetic framework face challenges due to cluster formation that prevents identification of unique populations of CIP, SIP, and SSIP pairing. Incorporation of such a multi-step kinetic modeling approach to accommodate the clusters is described by Chen and Pappu[78].

Finally, we provide a few comments on how our detailed MD results on ion-pairing in the GAG brush relate to current knowledge and theories of ion condensation on polyelectrolytes. Counterion condensation theory developed by Manning recognized the need to consider the pairing of counterions when the polyelectrolyte charges are closely-spaced and described how the condensation depends on Debye and Bjerrum length scales.[79–81] The theory has been widely applied for decades to polyelectrolytes including ionizable osmotic brushes, but it breaks down in the high-salt limit[82] and does not adequately address the details of ion-specific behavior for different salts. Ion-pairing has been shown to depend sensitively on the SIP-CIP dynamic equilibria, hydration, and ion-exchange specifics that are absent from the earlier condensation theory as well as continuum electrostatic models with fixed water dielectric constant. We refer the reader to a thorough discussion of these salient issues by Yu, Pettitt, and Iwahara[83] who explain how ions interact at nucleic acid backbone phosphates. They address recent results of "ion counting" experimental methods that quantify ion-pairing and anion exclusion and describe shortcomings of condensation theory, Poisson-Boltzmann theory, integral molecular solvation theory, and implicit solvent MD models. We contend that all-atom explicit water MD simulations represent an important advance not only in understanding ion-specific-pairing behavior, but in the development of mean-field models that incorporate such behavior.

CONCLUSIONS

The results of the all atom MD simulations of GAG brushes presented here show ion-specific behavior with energy contributions associated with Born-hydration, electrostatic, and ion-pair binding energies that are of similar magnitude. The results demonstrate that sulfates bind to Na^+ and K^+ approximately half as tightly as carboxylates, but heparin with 4x the number of sulfates as carboxylates results in ion binding that is dependent on the multivalent integral charge density with minimal cooperativity of the binding. Furthermore, the radial distribution functions of ion-pairing show similar abundance of CIP and SIP forms for all combinations of cations and GAG anions. Our results suggest that mean-field models require inclusion of both ion-pair binding energy and Born hydration using water dielectric constant variation that varies in space and time. We would expect that such a model could describe emergent brush biophysics on length scales substantially larger than the Debye length. Thus, modified Poisson-Boltzmann models including local ion-pairing through law of mass action could be used for quasi-equilibria[26,62]; and Poisson's equation of electrostatics coupled with Nernst-Planck (PNP) models of transport of ions due to

electrophoresis and diffusion, and bimolecular Eigen-Tamm ion-pairing reactions might be used to describe transient MD results.[67,68,74,78] The balances and tradeoffs of electrostatic, ion-binding, and Born-hydration energy terms could have important implications for both *in vitro* and *in vivo* systems that apply to electrophysiology, tissue engineering, separation science, therapeutics and medical device engineering.

AUTHOR INFORMATION

The authors declare no competing financial interests.

SUPPORTING INFORMATION

Includes a table of all systems simulated showing glycan type, total charge, number of each atom and duration of each simulation; a table of all ion pair Lennard-Jones simulation parameters; a figure showing the average z-axis charge density profiles for 6, 8, 12, and 16 disaccharide heparin brushes in NaCl; figures showing the radial distribution functions (RDF) for heparin anionic group center to sodium and potassium cations; figures showing RDF curves for hyaluronan with sodium and potassium cations based on oxygen-cation distances and carbon-cation distances. Also includes a set of six figures showing convergence to quasi-steady state over 100ns for the CHARMM36 force fields and over 40ns for the Drude force field; figures illustrating the RDF for heparin-carboxylate and the Donnan potential in the brush with- and without the LJ corrections in the NBFIX parameters. Finally includes computational details and description of standard deviation equations used and additional references relevant to SI.

ACKNOWLEDGMENT

J.D.S acknowledges support from the Keck Graduate Institute faculty research fund and Y.L.L. acknowledges the support from NIH Grant R01-GM130834. Computational resources were provided via the Extreme Science and Engineering Discovery Environment (XSEDE) allocation TG-MCB160119, which is supported by NSF grant number ACI-154862. The authors acknowledge very helpful conversations with Prof. Ali Nadim and Dr. Shenda Baker regarding the biophysical and polymer science aspects of this work. The authors also wish to thank the Prof. Alex MacKerell group, in particular Dr. Asaminew Haile Aytenfisu for assistance with the Drude model and Prof. Justin Lemkul for discussions regarding the NBFIX parameters in the Drude model.

REFERENCES

(1) Minsky, B. B.; Dubin, P. L.; Kaltashov, I. A. Electrostatic Forces as Dominant Interactions Between Proteins and Polyanions: An ESI MS Study of Fibroblast Growth Factor Binding to Heparin Oligomers. *J. Am. Soc. Mass Spectrom.* **2017**, *28* (4), 758–767. https://doi.org/10.1007/s13361-017-1596-0.

(2) Zimmermann, R.; Werner, C.; Sterling, J. Exploring Structure–Property Relationships of GAGs to Tailor ECM-Mimicking Hydrogels. *Polymers* **2018**, *10* (12), 1376. https://doi.org/10.3390/polym10121376.

(3) Freudenberg, U.; Atallah, P.; Limasale, Y. D. P.; Werner, C. Charge-Tuning of Glycosaminoglycan-Based Hydrogels to Program Cytokine Sequestration. *Faraday Discuss.* **2019**, *219* (0), 244–251. https://doi.org/10.1039/C9FD00016J.

(4) Chiodelli, P.; Bugatti, A.; Urbinati, C.; Rusnati, M. Heparin/Heparan Sulfate Proteoglycans Glycomic Interactome in Angiogenesis: Biological Implications and Therapeutical Use. *Molecules* **2015**, *20* (4), 6342–6388. https://doi.org/10.3390/molecules20046342.

(5) Farrugia, B. L.; Lord, M. S.; Melrose, J.; Whitelock, J. M. The Role of Heparan Sulfate in Inflammation, and the Development of Biomimetics as Anti-Inflammatory Strategies: *Journal of Histochemistry & Cytochemistry.* **2018**. *66* (4), 321-336. https://doi.org/10.1369/0022155417740881.

(6) Collins, L. E.; Troeberg, L. Heparan Sulfate as a Regulator of Inflammation and Immunity. *Journal of Leukocyte Biology* **2019**, *105* (1), 81–92. https://doi.org/10.1002/JLB.3RU0618-246R.

(7) Verdurmen, W. P. R.; Wallbrecher, R.; Schmidt, S.; Eilander, J.; Bovee-Geurts, P.; Fanghänel, S.; Bürck, J.; Wadhwani, P.; Ulrich, A. S.; Brock, R. Cell Surface Clustering of Heparan Sulfate Proteoglycans by Amphipathic Cell-Penetrating Peptides Does Not Contribute to Uptake. *Journal of Controlled Release* **2013**, *170* (1), 83–91. https://doi.org/10.1016/j.jconrel.2013.05.001.

(8) Dam, T. K.; Brewer, F. C. Maintenance of Cell Surface Glycan Density by Lectin–Glycan Interactions: A Homeostatic and Innate Immune Regulatory Mechanism. *Glycobiology* **2010**, *20* (9), 1061–1064. https://doi.org/10.1093/glycob/cwq084.

(9) Xu, D.; Esko, J. D. Demystifying Heparan Sulfate-Protein Interactions. *Annu. Rev. Biochem.* **2014**, *83*, 129–157. https://doi.org/10.1146/annurev-biochem-060713-035314.

(10) Weiss, R. J.; Esko, J. D.; Tor, Y. Targeting Heparin– and Heparan Sulfate–Protein Interactions. *Org Biomol Chem* **2017**, *15* (27), 5656–5668. https://doi.org/10.1039/c7ob01058c.

(11) Ori, A.; Wilkinson, M. C.; Fernig, D. G. A Systems Biology Approach for the Investigation of the Heparin/Heparan Sulfate Interactome. *J Biol Chem* **2011**, *286* (22), 19892–19904. https://doi.org/10.1074/jbc.M111.228114.

(12) Bolten, S. N.; Rinas, U.; Scheper, T. Heparin: Role in Protein Purification and Substitution with Animal-Component Free Material. *Appl Microbiol Biotechnol* **2018**, *102* (20), 8647–8660. https://doi.org/10.1007/s00253-018-9263-3.

(13) Xiong, S.; Zhang, L.; He, Q.-Y. Fractionation of Proteins by Heparin Chromatography. *Methods Mol. Biol.* **2008**, *424*, 213–221. https://doi.org/10.1007/978-1-60327-064-9_18.

(14) Rauch, J. N.; Chen, J. J.; Sorum, A. W.; Miller, G. M.; Sharf, T.; See, S. K.; Hsieh-Wilson, L. C.; Kampmann, M.; Kosik, K. S. Tau Internalization Is Regulated by 6-O Sulfation on Heparan Sulfate Proteoglycans (HSPGs). *Sci Rep* **2018**, *8* (6382), 1-10. https://doi.org/10.1038/s41598-018-24904-z.

(15) Stopschinski, B. E.; Holmes, B. B.; Miller, G. M.; Manon, V. A.; Vaquer-Alicea, J.; Prueitt, W. L.; Hsieh-Wilson, L. C.; Diamond, M. I. Specific Glycosaminoglycan Chain Length and Sulfation Patterns Are Required for Cell Uptake of Tau versus α-Synuclein and β-Amyloid Aggregates. *J. Biol. Chem.* **2018**, *293* (27), 10826–10840. https://doi.org/10.1074/jbc.RA117.000378.
(16) Mycroft-West, C. J.; Su, D.; Pagani, I.; Rudd, T. R.; Elli, S.; Gandhi, N. S.; Guimond, S. E.; Miller, G.; Meneghetti, M. C. Z.; Nader, H. B.; et al., M. A. Heparin Inhibits Cellular Invasion by SARS-CoV-2: Structural Dependence of the Spike S1 Receptor-Binding Domain with Heparin. *Thromb. Haemost.* **2020**, *120* (12), 1700–1715. https://doi.org/10.1055/s-0040-1721319.
(17) Cagno, V.; Tseligka, E. D.; Jones, S. T.; Tapparel, C. Heparan Sulfate Proteoglycans and Viral Attachment: True Receptors or Adaptation Bias? *Viruses* **2019**, *11* (7), 596. https://doi.org/10.3390/v11070596.
(18) Park, S.; Barnes, R.; Lin, Y.; Jeon, B.; Najafi, S.; Delaney, K. T.; Fredrickson, G. H.; Shea, J.-E.; Hwang, D. S.; Han, S. Dehydration Entropy Drives Liquid-Liquid Phase Separation by Molecular Crowding. *Communications Chemistry* **2020**, *3* (1), 1–12. https://doi.org/10.1038/s42004-020-0328-8.
(19) Sterling, J. D.; Baker, S. M. A Continuum Model of Mucosa with Glycan-Ion Pairing. *Macromolecular Theory and Simulations* **2018**, *27* (2), 1700079. https://doi.org/10.1002/mats.201700079.
(20) Dukhin, S. S.; Zimmermann, R.; Werner, C. Intrinsic Charge and Donnan Potentials of Grafted Polyelectrolyte Layers Determined by Surface Conductivity Data. *J Colloid Interface Sci* **2004**, *274* (1), 309–318. https://doi.org/10.1016/j.jcis.2003.11.016.
(21) Barbati, A. C.; Kirby, B. J. Soft Diffuse Interfaces in Electrokinetics – Theory and Experiment for Transport in Charged Diffuse Layers. *Soft Matter* **2012**, *8* (41), 10598–10613. https://doi.org/10.1039/C2SM26121A.
(22) Schnitzer, J. E. Glycocalyx Electrostatic Potential Profile Analysis: Ion, PH, Steric, and Charge Effects. *Yale J Biol Med* **1988**, *61* (5), 427–446.
(23) Stace, T. M.; Damiano, E. R. An Electrochemical Model of the Transport of Charged Molecules through the Capillary Glycocalyx. *Biophys J* **2001**, *80* (4), 1670–1690.
(24) Zimmermann, R.; Kuckling, D.; Kaufmann, M.; Werner, C.; Duval, J. F. L. Electrokinetics of a Poly(N-Isopropylacrylamid-Co-Carboxyacrylamid) Soft Thin Film: Evidence of Diffuse Segment Distribution in the Swollen State. *Langmuir* **2010**, *26* (23), 18169–18181. https://doi.org/10.1021/la103526b.
(25) Zimmermann, R.; Gunkel-Grabole, G.; Bünsow, J.; Werner, C.; Huck, W. T. S.; Duval, J. F. L. Evidence of Ion-Pairing in Cationic Brushes from Evaluation of Brush Charging and Structure by Electrokinetic and Surface Conductivity Analysis. *J. Phys. Chem. C* **2017**, *121* (5), 2915–2922. https://doi.org/10.1021/acs.jpcc.6b12531.
(26) Sterling, J. D.; Baker, S. M. Electro-Lyotropic Equilibrium and the Utility of Ion-Pair Dissociation Constants. *Colloid and Interface Science Communications* **2017**, *20*, 9–11. https://doi.org/10.1016/j.colcom.2017.08.002.
(27) Xu, X.; Mastropietro, D.; Ruths, M.; Tirrell, M.; Yu, J. Ion-Specific Effects of Divalent Ions on the Structure of Polyelectrolyte Brushes. *Langmuir* **2019**, *35* (48), 15564–15572. https://doi.org/10.1021/acs.langmuir.9b01984.

(28) Aytenfisu, A. H.; Yang, M.; MacKerell, A. D. CHARMM Drude Polarizable Force Field for Glycosidic Linkages Involving Pyranoses and Furanoses. *J. Chem. Theory Comput.* **2018**, *14* (6), 3132–3143. https://doi.org/10.1021/acs.jctc.8b00175.
(29) M, Y.; Ah, A.; Jr, M. A. Proper Balance of Solvent-Solute and Solute-Solute Interactions in the Treatment of the Diffusion of Glucose Using the Drude Polarizable Force Field. *Carbohydr Res* **2018**, *457*, 41–50. https://doi.org/10.1016/j.carres.2018.01.004.
(30) Patel, D. S.; He, X.; MacKerell, A. D. Polarizable Empirical Force Field for Hexopyranose Monosaccharides Based on the Classical Drude Oscillator. *J Phys Chem B* **2015**, *119* (3), 637–652. https://doi.org/10.1021/jp412696m.
(31) He, X.; Lopes, P. E. M.; MacKerell, A. D. Polarizable Empirical Force Field for Acyclic Polyalcohols Based on the Classical Drude Oscillator. *Biopolymers* **2013**, *99* (10), 724–738. https://doi.org/10.1002/bip.22286.
(32) Pandey, P.; Aytenfisu, A. H.; MacKerell, A. D.; Mallajosyula, S. S. Drude Polarizable Force Field Parametrization of Carboxylate and N-Acetyl Amine Carbohydrate Derivatives. *J Chem Theory Comput* **2019**, *15* (9), 4982–5000. https://doi.org/10.1021/acs.jctc.9b00327.
(33) Pincus, P. Colloid Stabilization with Grafted Polyelectrolytes. *Macromolecules* **1991**, *24* (10), 2912–2919. https://doi.org/10.1021/ma00010a043.
(34) Farina, R.; Laugel, N.; Pincus, P.; Tirrell, M. Brushes of Strong Polyelectrolytes in Mixed Mono- and Tri-Valent Ionic Media at Fixed Total Ionic Strengths. *Soft Matter* **2013**, *9* (44), 10458. https://doi.org/10.1039/c3sm51450a.
(35) Wang, H. M.; Loganathan, D.; Linhardt, R. J. Determination of the PKa of Glucuronic Acid and the Carboxy Groups of Heparin by 13C-Nuclear-Magnetic-Resonance Spectroscopy. *Biochemical Journal* **1991**, *278* (3), 689–695. https://doi.org/10.1042/bj2780689.
(36) Mallajosyula, S. S.; Guvench, O.; Hatcher, E.; MacKerell, A. D. CHARMM Additive All-Atom Force Field for Phosphate and Sulfate Linked to Carbohydrates. *J Chem Theory Comput* **2012**, *8* (2), 759–776. https://doi.org/10.1021/ct200792v.
(37) Guvench, O.; Hatcher, E.; Venable, R. M.; Pastor, R. W.; MacKerell, A. D. CHARMM Additive All-Atom Force Field for Glycosidic Linkages between Hexopyranoses. *J. Chem. Theory Comput.* **2009**, *5* (9), 2353–2370. https://doi.org/10.1021/ct900242e.
(38) Raman, E. P.; Guvench, O.; MacKerell, A. D. CHARMM Additive All-Atom Force Field for Glycosidic Linkages in Carbohydrates Involving Furanoses. *J Phys Chem B* **2010**, *114* (40), 12981–12994. https://doi.org/10.1021/jp105758h.
(39) Guvench, O.; Mallajosyula, S. S.; Raman, E. P.; Hatcher, E.; Vanommeslaeghe, K.; Foster, T. J.; Jamison, F. W.; Mackerell, A. D. CHARMM Additive All-Atom Force Field for Carbohydrate Derivatives and Its Utility in Polysaccharide and Carbohydrate-Protein Modeling. *J Chem Theory Comput* **2011**, *7* (10), 3162–3180. https://doi.org/10.1021/ct200328p.
(40) Yoo, J.; Aksimentiev, A. Improved Parametrization of Li+, Na+, K+, and Mg2+ Ions for All-Atom Molecular Dynamics Simulations of Nucleic Acid Systems. *J. Phys. Chem. Lett.* **2012**, *3* (1), 45–50. https://doi.org/10.1021/jz201501a.
(41) Jo, S.; Kim, T.; Iyer, V. G.; Im, W. CHARMM-GUI: A Web-Based Graphical User Interface for CHARMM. *Journal of Computational Chemistry* **2008**, *29* (11), 1859–1865. https://doi.org/10.1002/jcc.20945.
(42) Jo, S.; Song, K. C.; Desaire, H.; MacKerell, A. D.; Im, W. Glycan Reader: Automated Sugar Identification and Simulation Preparation for Carbohydrates and Glycoproteins. *J Comput Chem* **2011**, *32* (14), 3135–3141. https://doi.org/10.1002/jcc.21886.

(43) Park, S.-J.; Lee, J.; Patel, D. S.; Ma, H.; Lee, H. S.; Jo, S.; Im, W. Glycan Reader Is Improved to Recognize Most Sugar Types and Chemical Modifications in the Protein Data Bank. *Bioinformatics* **2017**, *33* (19), 3051–3057. https://doi.org/10.1093/bioinformatics/btx358.

(44) Park, S.-J.; Lee, J.; Qi, Y.; Kern, N. R.; Lee, H. S.; Jo, S.; Joung, I.; Joo, K.; Lee, J.; Im, W. CHARMM-GUI Glycan Modeler for Modeling and Simulation of Carbohydrates and Glycoconjugates. *Glycobiology* **2019**, *29* (4), 320–331. https://doi.org/10.1093/glycob/cwz003.

(45) Pronk, S.; Páll, S.; Schulz, R.; Larsson, P.; Bjelkmar, P.; Apostolov, R.; Shirts, M. R.; Smith, J. C.; Kasson, P. M.; van der Spoel, D.; et al. GROMACS 4.5: A High-Throughput and Highly Parallel Open Source Molecular Simulation Toolkit. *Bioinformatics* **2013**, *29* (7), 845–854. https://doi.org/10.1093/bioinformatics/btt055.

(46) Jorgensen, W. L.; Chandrasekhar, J.; Madura, J. D.; Impey, R. W.; Klein, M. L. Comparison of Simple Potential Functions for Simulating Liquid Water. *J. Chem. Phys.* **1983**, *79* (2), 926–935. https://doi.org/10.1063/1.445869.

(47) Venable, R. M.; Luo, Y.; Gawrisch, K.; Roux, B.; Pastor, R. W. Simulations of Anionic Lipid Membranes: Development of Interaction-Specific Ion Parameters and Validation Using NMR Data. *J. Phys. Chem. B* **2013**, *117* (35), 10183–10192. https://doi.org/10.1021/jp401512z.

(48) Lamoureux, G.; Harder, E.; Vorobyov, I. V.; Roux, B.; MacKerell, A. D. A Polarizable Model of Water for Molecular Dynamics Simulations of Biomolecules. *Chemical Physics Letters* **2006**, *418* (1), 245–249. https://doi.org/10.1016/j.cplett.2005.10.135.

(49) Essmann, U.; Perera, L.; Berkowitz, M. L.; Darden, T.; Lee, H.; Pedersen, L. G. A Smooth Particle Mesh Ewald Method. *J. Chem. Phys.* **1995**, *103* (19), 8577–8593. https://doi.org/10.1063/1.470117.

(50) Aksimentiev, A.; Schulten, K. Imaging α-Hemolysin with Molecular Dynamics: Ionic Conductance, Osmotic Permeability, and the Electrostatic Potential Map. *Biophys J* **2005**, *88* (6), 3745–3761. https://doi.org/10.1529/biophysj.104.058727.

(51) Bazant, M. Z.; Kilic, M. S.; Storey, B. D.; Ajdari, A. Towards an Understanding of Induced-Charge Electrokinetics at Large Applied Voltages in Concentrated Solutions. *Advances in Colloid and Interface Science* **2009**, *152* (1), 48–88. https://doi.org/10.1016/j.cis.2009.10.001.

(52) Grahame, D. C. Effects of Dielectric Saturation upon the Diffuse Double Layer and the Free Energy of Hydration of Ions. *J. Chem. Phys.* **1950**, *18* (7), 903–909. https://doi.org/10.1063/1.1747807.

(53) Gupta, A.; Stone, H. A. Electrical Double Layers: Effects of Asymmetry in Electrolyte Valence on Steric Effects, Dielectric Decrement, and Ion–Ion Correlations. *Langmuir* **2018**, *34* (40), 11971–11985. https://doi.org/10.1021/acs.langmuir.8b02064.

(54) López-García, J. J.; Horno, J.; Grosse, C. Multiionic and Permittivity-Related Effects on the Diffuse Electric Double Layer Structure at Solid-Electrolyte Solution Interfaces. *Adv. in Mat. Sci. and Eng.* **2018** *2018* (432216894), 1-11. https://doi.org/10.1155/2018/4316894.

(55) Vezzani, D.; Bandini, S. Donnan Equilibrium and Dielectric Exclusion for Characterization of Nanofiltration Membranes. *Desalination* **2002**, *149* (1), 477–483. https://doi.org/10.1016/S0011-9164(02)00784-1.

(56) Stirnemann, G.; Wernersson, E.; Jungwirth, P.; Laage, D. Mechanisms of Acceleration and Retardation of Water Dynamics by Ions. *J. Am. Chem. Soc.* **2013**, *135* (32), 11824–11831. https://doi.org/10.1021/ja405201s.
(57) Ben-Yaakov, D.; Andelman, D.; Podgornik, R. Dielectric Decrement as a Source of Ion-Specific Effects. *J. Chem. Phys.* **2011**, *134* (074705), 1-12. https://doi.org/10.1063/1.3549915.
(58) Hribar, B.; Southall, N. T.; Vlachy, V.; Dill, K. A. How Ions Affect the Structure of Water. *J. Am. Chem. Soc.* **2002**, *124* (41), 12302–12311. https://doi.org/10.1021/ja026014h.
(59) Andreev, M.; de Pablo, J. J.; Chremos, A.; Douglas, J. F. Influence of Ion Solvation on the Properties of Electrolyte Solutions. *The Journal of Physical Chemistry B* **2018**, *122* (14), 4029–4034. https://doi.org/10.1021/acs.jpcb.8b00518.
(60) Gun'ko, V. M.; Savina, I. N.; Mikhalovsky, S. V. Properties of Water Bound in Hydrogels. *Gels* **2017**, *3* (37), 1-30. https://doi.org/10.3390/gels3040037.
(61) van der Vegt, N. F. A.; Haldrup, K.; Roke, S.; Zheng, J.; Lund, M.; Bakker, H. J. Water-Mediated Ion Pairing: Occurrence and Relevance. *Chem. Rev.* **2016**, *116* (13), 7626–7641. https://doi.org/10.1021/acs.chemrev.5b00742.
(62) Boström, M.; Williams, D. R. M.; Ninham, B. Specific Ion Effects: Why DLVO Theory Fails for Biology and Colloid Systems. *Physical review letters* **2001**, *87* (168103), 1-4. https://doi.org/10.1103/PhysRevLett.87.168103.
(63) Lo Nostro, P.; Ninham, B. W. Hofmeister Phenomena: An Update on Ion Specificity in Biology. *Chem Rev* **2012**, *112* (4), 2286–2322. https://doi.org/10.1021/cr200271j.
(64) Seal, S.; Doblhoff-Dier, K.; Meyer, J. Dielectric Decrement for Aqueous NaCl Solutions: Effect of Ionic Charge Scaling in Nonpolarizable Water Force Fields. *J Phys Chem B* **2019**, *123* (46), 9912–9921. https://doi.org/10.1021/acs.jpcb.9b07916.
(65) Kirby, B. J.; Jungwirth, P. Charge Scaling Manifesto: A Way of Reconciling the Inherently Macroscopic and Microscopic Natures of Molecular Simulations. *J. Phys. Chem. Lett.* **2019**, *10* (23), 7531–7536. https://doi.org/10.1021/acs.jpclett.9b02652.
(66) Tolmachev, D. A.; Boyko, O. S.; Lukasheva, N. V.; Martinez-Seara, H.; Karttunen, M. Overbinding and Qualitative and Quantitative Changes Caused by Simple Na+ and K+ Ions in Polyelectrolyte Simulations: Comparison of Force Fields with and without NBFIX and ECC Corrections. *J. Chem. Theory Comput.* **2020**, *16* (1), 677–687. https://doi.org/10.1021/acs.jctc.9b00813.
(67) Marcus, Y.; Hefter, G. Ion Pairing. *Chem. Rev.* **2006**, *106* (11), 4585–4621. https://doi.org/10.1021/cr040087x.
(68) Roy, S.; Baer, M. D.; Mundy, C. J.; Schenter, G. K. Marcus Theory of Ion-Pairing. *J. Chem. Theory Comput.* **2017**, *13* (8), 3470–3477. https://doi.org/10.1021/acs.jctc.7b00332.
(69) Zhulina, E. B.; Birshtein, T. M.; Borisov, O. V. Theory of Ionizable Polymer Brushes. *Macromolecules* **1995**, *28* (5), 1491–1499. https://doi.org/10.1021/ma00109a021.
(70) Dzubiella, J.; Fyta, M.; Horinek, D.; Kalcher, I.; Netz, R. R.; Schwierz, N. Ion-Specificity: From Solvation Thermodynamics to Molecular Simulations and Back. In *Specific Ion Effects*; WORLD SCIENTIFIC, 2009; 231–265. https://doi.org/10.1142/9789814271585_0009.
(71) Collins, K. D. The Behavior of Ions in Water Is Controlled by Their Water Affinity. *Quarterly Reviews of Biophysics* **2019**, *52,* e11, 1-19. https://doi.org/10.1017/S0033583519000106.

(72) Nagarajan, A.; Malvi, P.; Wajapeyee, N. Heparan Sulfate and Heparan Sulfate Proteoglycans in Cancer Initiation and Progression. *Front. Endocrinol.* **2018**, *9* (483),1-11. https://doi.org/10.3389/fendo.2018.00483.

(73) Lawrence, R.; Yabe, T.; HajMohammadi, S.; Rhodes, J.; McNeely, M.; Liu, J.; Lamperti, E. D.; Toselli, P. A.; Lech, M.; Spear, P. G.; et al. The Principal Neuronal GD-Type 3-O-Sulfotransferases and Their Products in Central and Peripheral Nervous System Tissues. *Matrix Biol* **2007**, *26* (6), 442–455. https://doi.org/10.1016/j.matbio.2007.03.002.

(74) Eigen, M.; Tamm, K. Schallabsorption in Elektrolytlösungen als Folge chemischer Relaxation I. Relaxationstheorie der mehrstufigen Dissoziation. *Zeitschrift für Elektrochemie, Berichte der Bunsengesellschaft für physikalische Chemie* **1962**, *66* (2), 93–107. https://doi.org/10.1002/bbpc.19620660205.

(75) Boda, D.; Henderson, D.; Gillespie, D. The Role of Solvation in the Binding Selectivity of the L-Type Calcium Channel. *J Chem Phys* **2013**, *139* (005103), 1-10. https://doi.org/10.1063/1.4817205.

(76) Liu, X.; Lu, B. Incorporating Born Solvation Energy into the Three-Dimensional Poisson-Nernst-Planck Model to Study Ion Selectivity in KcsA K^+ Channels. *Phys. Rev. E* **2017**, *96* (062416), 1-10. https://doi.org/10.1103/PhysRevE.96.062416.

(77) Fennell, C. J.; Bizjak, A.; Vlachy, V.; Dill, K. A. Ion Pairing in Molecular Simulations of Aqueous Alkali Halide Solutions. *J. Phys. Chem. B* **2009**, *113* (19), 6782–6791. https://doi.org/10.1021/jp809782z.

(78) Chen, A. A.; Pappu, R. V. Quantitative Characterization of Ion Pairing and Cluster Formation in Strong 1:1 Electrolytes. *J. Phys. Chem. B* **2007**, *111* (23), 6469–6478. https://doi.org/10.1021/jp0708547.

(79) Manning, G. S. Limiting Laws and Counterion Condensation in Polyelectrolyte Solutions I. Colligative Properties. *J. Chem. Phys.* **1969**, *51* (3), 924–933. https://doi.org/10.1063/1.1672157.

(80) Manning, G. S. Limiting Laws and Counterion Condensation in Polyelectrolyte Solutions. III. An Analysis Based on the Mayer Ionic Solution Theory. *J. Chem. Phys.* **1969**, *51* (8), 3249–3252. https://doi.org/10.1063/1.1672502.

(81) Manning, G. S. Limiting Laws and Counterion Condensation in Polyelectrolyte Solutions: IV. The Approach to the Limit and the Extraordinary Stability of the Charge Fraction. *Biophysical Chemistry* **1977**, *7* (2), 95–102. https://doi.org/10.1016/0301-4622(77)80002-1.

(82) Deserno, M.; Holm, C.; May, S. Fraction of Condensed Counterions around a Charged Rod: Comparison of Poisson−Boltzmann Theory and Computer Simulations. *Macromolecules* **2000**, *33* (1), 199–206. https://doi.org/10.1021/ma990897o.

(83) Yu, B.; Pettitt, B. M.; Iwahara, J. Dynamics of Ionic Interactions at Protein–Nucleic Acid Interfaces. *Acc Chem Res* **2020**, *53* (9), 1802–1810. https://doi.org/10.1021/acs.accounts.0c00212.

TOC GRAPHIC

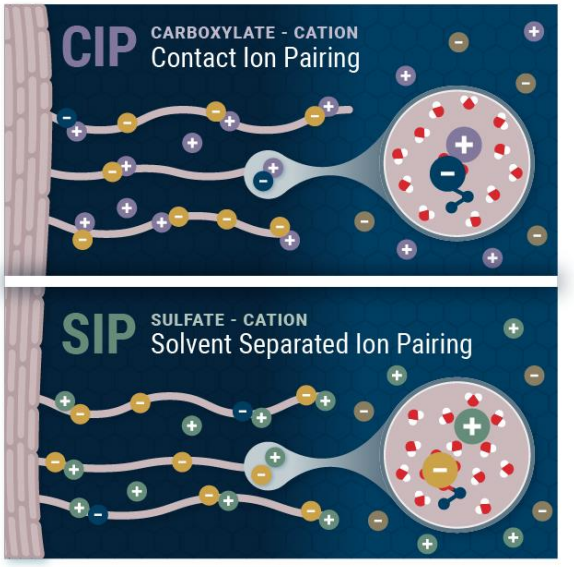

KEYWORDS glycosaminoglycan, Donnan potential, Born solvation, dielectric decrement, polyelectrolyte brush